ARMA 24–1005

Destruction of Rock Microstructure: an Experimental and Numerical Modelling Study of High-Pressure Water Jet Rock Cutting under Subsurface Confining Pressure Conditions

Xiang, X., Naderi, S. and Latham, J-P.

Earth Science and Engineering Department, Imperial College London, London, UK

Gerbaud, L., Velmurugan, N., Thenevin, I. and Sellami, H.

Mines Paris, PSL University, Center for geosciences and geoengineering, Fontainebleau, France

ABSTRACT: High Pressure Water Jetting (HPWJ) can be applied at the drill bit-rock interface and is especially promising for deep highly confined geothermal reservoir rocks if used for peripheral groove cutting in the bottom hole. The groove can greatly reduce the mean stress making the work of the percussive hammer drill easier and faster. A numerical FDEM model of the jet loading and mineral fragment removal of a coarse-grained granite under confining pressure is introduced. The loading of a 1 mm nozzle delivering a 240 MPa jet is modelled using a spatio-temporal pressure distribution. A quartz-feldspar-mica Voronoi-based microstructure of the Sidobre granite with inter- and intra-grain properties was calibrated. A non-traversing jetting test performed in a confining pressure cell rig was used to calibrate the jet-rock interaction model which applies a defect intensity parameter. The model matched the 4-6 mm experimental groove depths for the validation study benchmark conditions of a rotating jet traversing at 157 mm/s (20 RPM) with 20 MPa back pressure. We observe a spectrum of groove or crater depths with widths normally more than twice the depth. These variations are influenced by factors such as the jet's starting point, crystalline topology, and the local mineral phases.

1. INTRODUCTION

Technological innovation in drilling deeper faster is widely cited as the key requirement to unlocking greater investment in deep geothermal energy. The ORCHYD project (https://www.orchyd.eu/) introduces a hybrid technology that employs a high-pressure water jet (HPWJ) to create a peripheral groove together with the percussive action of a mud hammer. Stress analysis of the bottom hole suggests grooves of approximately 20 mm in depth will considerably lower the mean stress state of the rock being loaded by repeated blows, hence lowering the rock's resistance to brittle failure. But the positive stress-relief effect of the groove is increasingly more difficult to achieve the deeper we drill, because increased backpressure and in-situ confining stress make it more difficult to jet a sufficiently deep groove. Geothermal drilling is increasingly targeting deep ~4-6 km rock. Experiments (Stoxreiter et al., 2019) suggest that it is possible to overcome 50 MPa of backpressure and the resistance to fracture of tough rocks like granites if: (i) a jet is from a nozzle chamber pressure with at least 220 MPa for the case of 50 MPa back pressure, (ii) there is enough hydraulic power at the rock surface, and (iii) the jet does not transverse too fast. The operational conditions of the jetting system downhole that are needed to cut rock grooves in different rock and in-situ conditions in the most effective way, remains poorly understood. In this work, we develop a predictive model to help optimise groove depth under the physical conditions of deep geothermal drilling, i.e., conditions beyond the realm of laboratory experiments.

2. METHODOLOGY: FDEM SIMULATION OF HPWJ USING SOLIDITY

2.1. Introduction to FDEM

In FDEM (i.e., also known as FEMDEM), the domain is treated as a multi-body system, with each discrete element further discretised into finite elements. FDEM analyses the discontinuum behaviour, such as multi-body interactions and contacts at fracture surfaces, while the continuum behaviour, including deformation and stress within discrete elements, is analysed using FEM. The intact material is initially modelled as a continuum using FEM, and after fracture initiation, a mix of continua and fractures is considered, with FEM remaining in the continua and DEM handling the interaction between discrete fracture surfaces using contact algorithms. Joint elements are assigned deformation and strength parameters, and their failure represents crack initiation. The stress increases elastically with joint aperture until reaching the strength threshold, followed by a nonlinear strain-softening stage. Transitioning from unbroken elasticity to a fully non-cohesive crack typically requires

3 to 4 joint elements. A Mohr-Coulomb criterion with a tension cut-off determines the shear strength based on the normal stress perpendicular to the shear direction. Additionally, the DEM formulation allows for handling large displacement problems efficiently.

The FDEM method, pioneered by Munjiza (2004) has been widely applied in a variety of engineering problems Xiang et al. (2009), Lei et al. (2014), Mahabadi et al. (2012). A full account of the 3D fracture model implemented in Solidity by Guo and Xiang in 2014 can be found in Guo's PhD Thesis and in shorter forms in Guo et al. (2015, 2020), with a mesh sensitivity study of Solidity FDEM presented in Guo et al. (2016).

The Mohr-Coulomb criterion with tensile cut-off is used together with fracture energy in the post-peak stress-displacement relationships for shear and tensile fracture. The solid rock mechanical (FDEM) model can then simulate the rock destruction process of the jet's hydraulic loading. For a microstructure-based model representation of the rock properties, the FDEM solver simulates the destruction process by modelling the cracking within minerals and along mineral boundaries. The crack coalescence and fragment formation and finally, fragment and chipping interactions and movement away from the intact rock to leave behind a crater or groove are all modelled. The fragment removal is reliably predicted to be the result of the jetting, provided the FDEM model has instructed the appropriate jet-induced forces to be applied at the boundary of the rock domain in the correct way, see Section 2.2 below. Also, if the model is for jetting in deep geothermal drilling conditions, representative bottom hole back pressures and geostatic stress states need to be applied correctly at the rock domain boundaries. Note that a continuum FEM solid model will not explicitly resolve the mechanics (i.e., motion and contact) of breaking pieces and their removal as fragments and chippings, whereas FDEM is ideal for these cases.

2.2. *Representation of HPWJ Destructive Forces as Pressure History Boundary Condition in FDEM Domain*

For a given nozzle chamber design with 1 mm diameter orifice, we first simulated the jet's exiting velocity profile. This profile was then used to simulate the pressure distribution impinging on the rock surface for the domain geometry and boundary conditions of the submerged jetting experiments performed in the pressure cell in the ARMINES laboratory in Pau, France, described in Latham et al. (2022). The CFD details were also presented in the same conference proceedings. Flow inside the pressure cell rig was computed with an adaptive meshing CFD code (IC-FERST) and the impinging pressure profiles were derived as shown in Figure 1. A quadratic best-fit function is used to generate the axisymmetric spatial distribution function of the impinging pressure to be used in the model.

The arrival of the jet on the surface happens very fast – within 0.1 of a msec and creates a strong water-hammer effect. It is possible to ramp the spatial pressure distribution over such a time, to reach the maximum impinging pressure distribution.

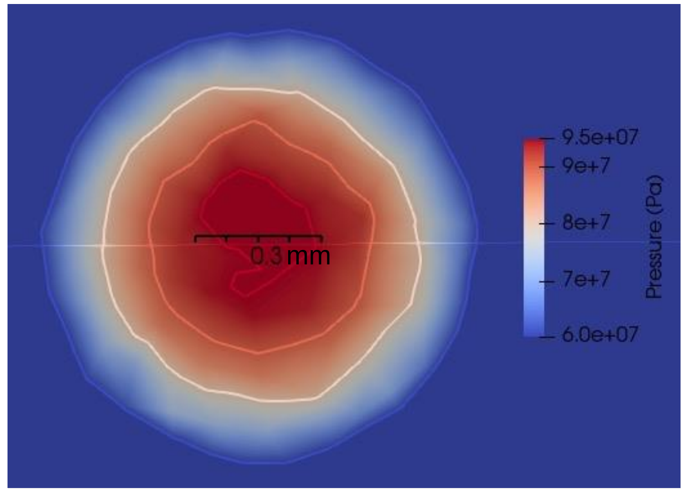

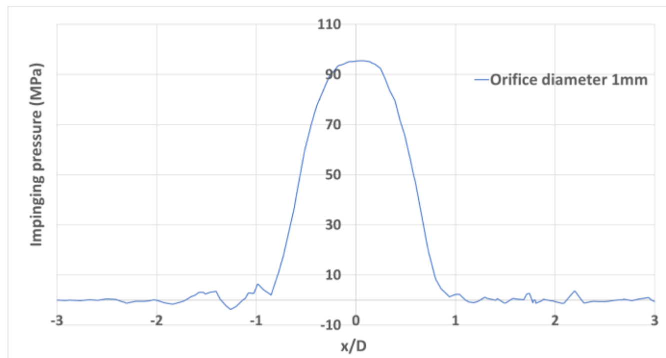

Fig 1. For standoff distance = 3 mm, nozzle diameter = 1 mm, nozzle chamber pressure = 100 MPa: (top) pressure contours of the bottom surface where jet impinges on rock; (bottom) pressure distribution along x direction on the bottom surface.

Due to the expensive CPU cost, this model is limited to a small-size simulation domain with short simulation time. Therefore, to simulate HPWJ within more reasonable run-times than full two-way coupled jet-rock models, see Xiang et al., (2022), a new one-way fluid-solid coupling model is developed and used in this research for ORCHYD, i.e., the fluid model (CFD) is separated from the solid model and pressure fields are treated as spatio-temporally varying boundary conditions to the solid model.

The pressure distribution as a function of radial distance from the jet axis that impinges on the flat surface of rock at a given standoff distance from the nozzle, as shown in Figure 1, can be idealised for different standoff distances, nozzle diameters and nozzle chamber pressures. This pressure distribution can be applied as a distributed loading to the solids model, for both a non-traversing jet and for the interesting case of a traversing jet. When the jet axis moves linearly or traces out a circular path such as when the jet is attached to the rotating bit, the pressure distribution can be applied as a moving loading boundary condition. Of course, once the rock surface starts to break up and create a crater or groove, the one-way coupled model becomes less accurate at describing the rock breakdown process. However, applying further simplifying assumptions, the jet pressure boundary condition can be modified to apply reasonably realistic loads while the rock surface and cratering evolves.

The FDEM model tracks all the dynamic and quasi-static crack initiation, propagation and fragment creation in space and time. A new algorithm was introduced to mimic the rock fragment removal during the fluid flushing action. The algorithm recognises all fragments (solid material bounded by broken element surface) and identifies those which will remain in position in the ongoing computation. It also allows the others which are sufficiently free, taking account of the fluid back pressure confinement, to be numerically removed immediately they become free, and these are logged under the category of 'removed fragments'. The simulation, at each time step, reveals the evolving new surfaces being created by the destructive jet actions. The pressure loading by the jet will continue to act normal to all newly exposed rock surface elements, or within small cavities, in accordance with the radial distance distribution for the given jet axis position. One further refinement implemented is that the pressure distribution is set to decay in strength according to the vertical distance from the nozzle and the decay is known to start once the standoff distance is 7 to 10 times the nozzle diameter.

2.3. Microstructure-Based FDEM Model

The Sidobre granite was selected as the "base case" granite type in the ORCHYD project and is a relatively coarsely grained granite. It is essential to consider that when subjected to local contact loading conditions of the jet in the range of 1 mm to 4 mm, the rock's response is likely to exhibit significant variability. This variability is dependent on the microstructural heterogeneity (i.e., granular structure configurations) of the rock immediately encountering the applied loads.

Granite, an igneous rock known for its durability and strength, is not exempt from the presence of structural features, including defects such as microcracks (e.g. Figure 2). These microcracks are minuscule fractures or fissures within the rock, often such that they remain imperceptible to the naked eye and may even elude detection under a microscope.

For shallow sub-surface rock engineering and in construction with rock-like geomaterials, crack propagation is commonly associated with tensile stress and tensile failure and the role of defects and micro-cracks acting as flaws and stress risers is well understood in fracture mechanics theory. For the deeper sub-surface, high in-situ bottom hole fluid pressures and confining stresses that will be experienced at drilling depths of say 4 to 5 km, the understanding of the role of microcracks is less clear.

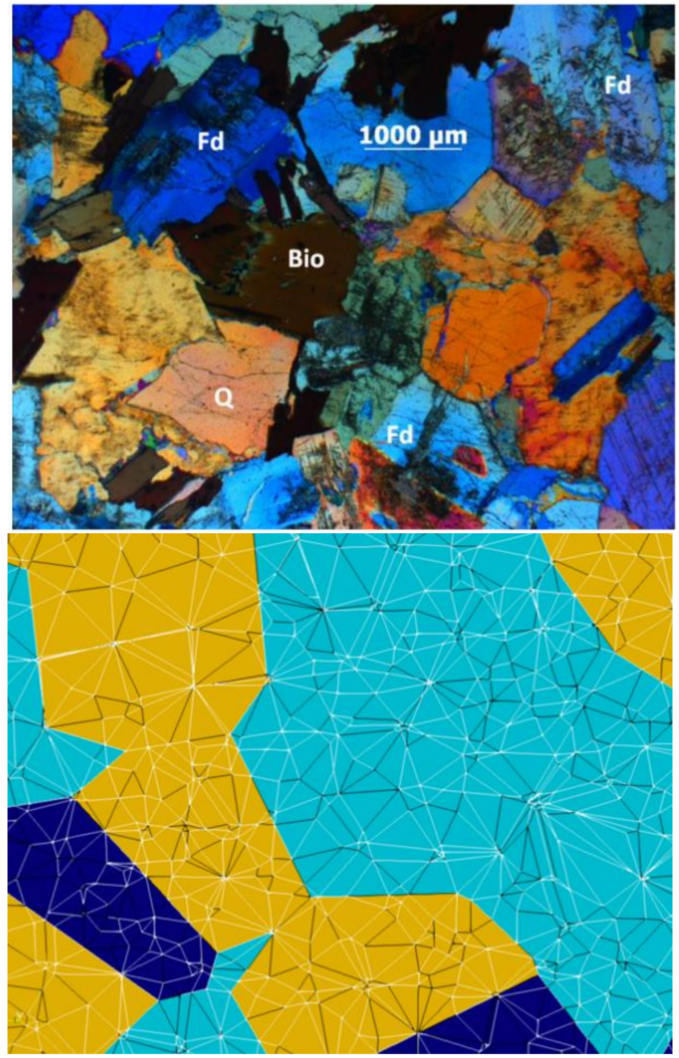

Fig 2. Defects in feldpar, quartz and biotite. (Top) Observations under cross-polarized light of the Sidobre (Silverstar) granite; (bottom) shown here is a 2D cross-sectional view of a 3D FDEM numerical model, where minerals are represented in different colours. The white line segments denote the traces of joint elements intersecting the cross-section, while the black segments signify the traces of pre-existing broken joint elements.

Microcracks/defects can be incorporated into FDEM numerical models by introducing pre-existing cracks as pre-broken joint elements - i.e., there is no effective joint element between tetrahedra. A numerical technique adopted here to avoid potential instability induced in the model is to reduce normal strength values of the joint elements by a factor of 100 or 1000.

The microstructure model is calibrated using an integrated experimental-numerical approach at three-levels: (i) nanoindentation for each phase, (ii) Brazilian disk to identify the tensile related parameters, and (iii) jetting to calibrate the shear related parameters. The process begins with the calibration and validation of a new model that incorporates microstructural features specific to Sidobre granite. In the final stage the characterised mechanical parameters can later be employed in Voronoi-based microstructure models (Zhang et al. 2019) for modelling the response to various loading scenarios.

In this work we generate representative microstructures of Sidobre granite within a small cubic volume of rock, situated within a larger cubic domain of homogeneous rock. The larger surrounding cube is assigned average engineering macroscopic density and elastic properties, representing an undamaged state – these properties are determined based on the new strength testing experiments as discussed in Dumoulin et al., (2024). The model described here constitutes a concurrent multiscale microstructure, as schematically illustrated in Figure 5 below.

3. EXPERIMENTAL DATA

3.1. Non-Traversing Tests for Validation

The jetting experiments used to calibrate and validate the microstructure-based jetting model for Sidobre Granite (SD) were conducted in the pressure cell at Pau and were designed for the purpose of calibrating the numerical model. The tests were carried out by rotating a rock in a pressurised cell where a high-pressure water jet was applied perpendicular to the rock surface at a radius of 7.5 cm from the axis of rotation. Throughout the test, the pressure inside the cell was controlled using a choke. To remove experimental uncertainties, the simplest reproducible setup (excluding the inevitable rock heterogeneity effects) and jet condition combined with the shortest simulation time was a short duration non-traversing jetting test. This would minimise the apparent uncertainties associated with the experimental rotation rate for short tests.

The time over which the jet is actively jetting on the same spot could not be controlled to a high level of accuracy for such short durations but could be back calculated. Knowing the results of such a coarse crystalline rock tend to vary widely from place to place it was essential also to try non-traversing jet grooving on several separate specimens (5 in all) of the rock and with four separate locations for each specimen to sample the variability. For the benchmark conditions of this test, Back Pressure 20 MPa, Chamber Pressure 240 MPa, Standoff Distance 4 mm and jet nozzle diameter 1.0 mm were applied. The scatter in maximum crater depth for a range of short durations are given in Figure 3.

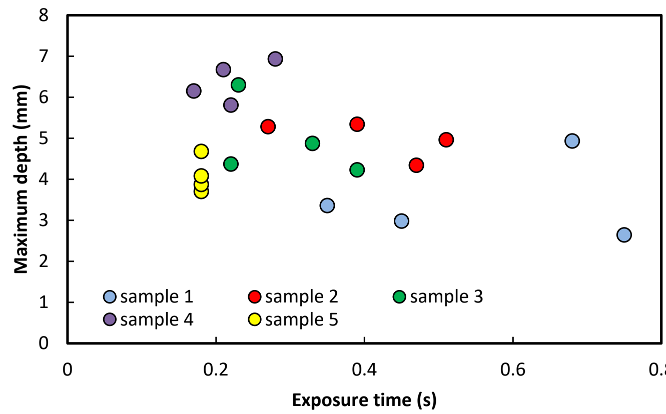

Fig. 3. Non-traversing jetting tests on Sidobre Granite (SD). For jetting conditions, see text.

3.2. Traversing Tests for Validation

The traversing tests employ a steel plate to protect the rock and focus jet-rock interaction within a series of 10 mm wide slots in the plate. Results of average maximum depth of traverse determined with laser-scan are presented in Figure 4.

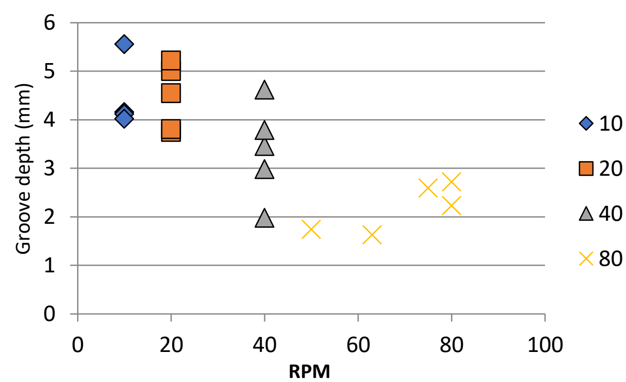

Fig. 4. Results of Depth of Groove for Benchmark testing conditions on SD rock at varying rotation rates. Note, at 20 RPM, traversing velocity is 0.157 m/s and for this condition, brown symbols correspond to the benchmark condition i.e., 20 MPa backpressure.

At 20 RPM the jet traverses the 10 mm open slots of exposed rock surface in just 0.063 s. Interestingly, a stationary jet acting for a duration of 0.2 s, some 3 times longer, makes a comparable depth crater. Traversing the jet is therefore more efficient in creating depth than a stationary jet, however when the jet traverses at increasingly faster rates, the groove depth reduces. The greatest depth is suggested by the experimental results in Figure 4 to be somewhere between 0 and 10 RPM.

3.3. Traversing Tests – from Parametric Study

A parametric study of variables affecting jetting depth resulting from nearly a full rotation of the jet include the results for Sidobre granite as shown in Figure 5.

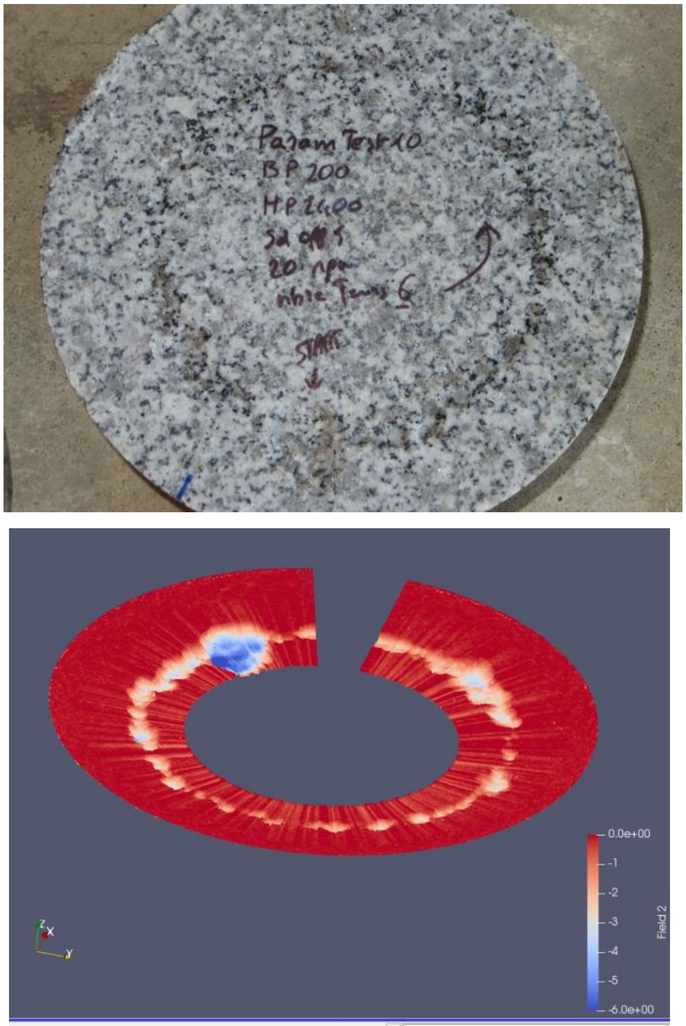

Fig. 5. Example of Sidobre Granite. The rock plate specimen under the influence of one full rotation of the HPWJ showing the surface "groove" and the starting point 'pit' and the graphical view (with opensource visualisation software Paraview) of the cratering and grooving data scan using the laser setup. Reported average minimum and maximum depth of groove is equal to 3 and 6 mm respectively, excluding the pit.

4. VALIDATION STUDY

It is very important to validate the numerical model before it is applied to simulate the HPWJ. In this research, the validation process has two levels:

1. The microstructure model is constructed, calibrated, and validated by 10 mm Brazilian indirect tensile tests.
2. The numerical model for HPWJ is further validated by jetting experimental tests under confinement. In this procedure, the Defect Intensity percentage parameter (DI) is calibrated. DI accounts for the microscopic scale defects and microcracks not represented by strength terms in the microstructural model and is defined as the percentage of pre-broken joint elements that are randomly assigned negligible strength. This procedure is described in the following section.

4.1. Calibration and Validation Process

The validation study consists of several stages. The benchmark case for jetting condition variables needs to be determined. Experimental and numerical model jetting duration time must be equivalent and for this it was agreed that ~0.2 s non-traversing jetting would be applied. The accuracy and precision (reliability) of the experimental result(s) for benchmarking is an important consideration. Then the most meaningful magnitudes of all the controllable jetting variables (back pressure, jet pressure etc.) are set as the benchmark conditions.

Experiments are performed with this set of base-line conditions forming the benchmarking case for the very specialised dynamic localised jetting application of the model.

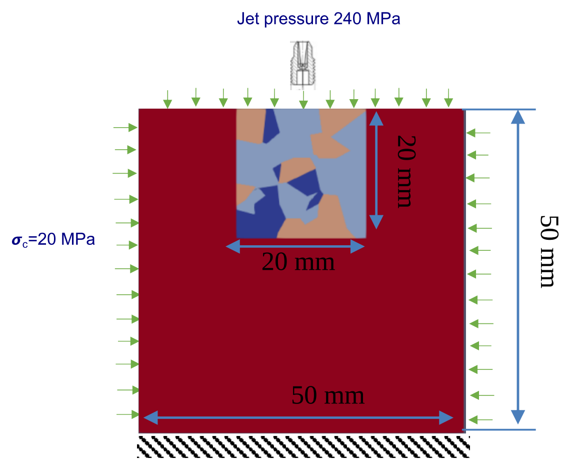

Fig. 6. Schematic of concurrent multiscale model, representing non-traversing jetting.

As seen in Figure 6, the model domain employs a concurrent multiscale model with a limited cubic volume for the crystal representation of interest. This cube is embedded in a surrounding medium of macroscopic average properties. Table 1 includes a row of properties labelled 'Macro'.

Numerical models of the jetting process are run for the benchmark case, first with the calibrated parameters that were validated for the 10 mm Brazilian disc compression tests as in Table 1, with no reference to engineering scale (~ 50 mm specimen) properties. The calibrated continuum properties of the pure mineral phases ρ, E, ν are assigned to the finite element tetrahedra. All other properties: friction coefficient Tan(ϕ), cohesion C, unconfined tensile strength T, Modes I and II critical energy release rates G_{IC}, G_{IIC}, are the fracturing-related strength variables for which calibrated parameters are assigned to the joint elements. There are several alternative roles played by the joint elements which act to represent potential fracture paths. These paths can be either within crystals (intra-grain) or along boundaries between crystals (inter-grain). Without invoking any defects, the jetting simulation finds the rock to be much too resistant to damage by jetting.

The details of the three-level calibration methodology are too lengthy to be adequately presented here. It involves integrating mineral mapping and nanoindentation tests, with collaboration from external university laboratories, specifically the University of Bristol. Subsequently, the material properties identified at the crystal level were utilised in the calibration of 10-millimeter Brazilian disks at the polycrystal level, as part of an upscaling strategy. Details are included in a paper in preparation by Naderi et al. 'AI-Assisted Multi-Level Characterisation of Crystalline Rock Mechanical Properties'. Explanatory details may also be accessed through publicly available deliverable reports (e.g., ORCHYD D5.4, 'Report on Numerical Modelling of Groove Jetting', 2024) on the ORCHYD project website, www.orchyd.eu.

Table 1**.** Material properties of the microstructure-based model of Sidobre Granite (SD).

Mineral/Interface	ρ (kg/m^3)	E (GPa)	ν	Tan(ϕ)	C (MPa)	T (MPa)	G_{IC} (N/m)	G_{IIC} (N/m)
Quartz	2650	48.19	0.17	1.746	126.98	18.70	11.60	34.80
Feldspar	2560	45.55	0.20	1.107	94.45	16.88	5.80	17.50
Biotite	3050	23.62	0.29	0.858	50.30	17.56	2.10	6.30
Quartz-Feldspar	-	-	-	0.343	77.50	6.225	3.05	18.30
Quartz-Biotite	-	-	-	0.318	62.05	12.69	2.4	14.40
Feldspar-Biotite	-	-	-	0.277	50.66	6.025	2.40	8.30
Macro	2630	67.30	0.27	1.080	22.9	8.90	0.1	1

A systematic study of the effect of DI in the range of 5-95% is then performed as discussed in Section 4.2 below. It is observed that the larger the DI, the deeper are the grooves generated. A value of 30% was selected for the DI parameter as it provides a good match when compared with the experiment – under benchmark conditions for the validation criterion used. Here we use maximum depth of groove. Other criteria such as volume of removed rock are also possible.

Our principal interest is in fact the destruction caused by a traversing jet. The traversing speed to be tested experimentally needs to be in the range of practical bit operations, a function of rotating bit RPM and radial distance from the nozzle orifice to the axis. It is then of great interest to evaluate whether the model calibration parameters validated for the non-traversing case can be used to predict grooving depths of the traversing jet experiments. For these time-limited tests, the jet is moving a total of about 5 mm at 157 mm/s. If traversing jet model results (calibrated with non-traversing test data as described above) prove to be good predictors of experimental results and of the trends comparing depths for non-traversing and traversing cases, that will provide the reassurance that the jetting model calibration is robust and valid for a significant range of velocities. The validated model can then be applied more widely e.g., to conduct a parametric study rather than just to the benchmark conditions. This can be referred to as 'Blind Test' prediction, for which there may or may not be any experimental data.

4.2. Sidobre Granite (SD) – Calibration of Defect Intensity (DI) for Non-Traversing Jet

The Model configuration was shown schematically in Fig. 6 as a concurrent model composed of the Voronoi-based microstructure of SD, which is embedded in a homogeneous domain. The green arrows symbolise the hydrostatic confining pressure boundary conditions such that bottom hole backpressures are 20 MPa as well as the horizontal and vertical confining pressure in the rock. The base of the rock cube is fixed to have zero displacement in all directions. Gravity is active. The jet's impinging pressure boundary condition (determined by CFD to be applicable to inlet velocities with the top hat profile for the 1 mm diameter orifice nozzle, driven by a chamber pressure of 240 MPa) is applied locally to the centre of the surface of the microstructure model domain. These conditions match those used in the pressure cell rig for the benchmark case. The example is provided for validation purposes, where back pressures of 20 MPa for a 2 km deep hole are reasonable, although the geostatic confining stresses would need to be about 2.5 times higher to be realistic for 2 km depth.

The *DI* parameter and the significance of having pre-broken joint elements, was introduced in Section 2.4. To illustrate the sensitivity of this parameter and how DI was calibrated for the non-traversing jetting case, see Figure 7. As *DI* as a percentage is increased from 20% to 25%, the jet action generates cracking to a greater depth but no further volume or depth of removed fragments is suggested along this line of section through the jet axis and crater. However, once *DI* is set at 30%, there is a sufficient increase in the numbers of joint elements with greatly reduced strength properties to promote cracking and fragments shown here as being removable. In this context a fragment is mineral material isolated by being surrounded by broken elements.

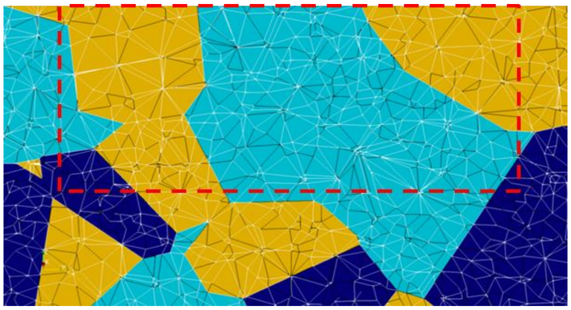

(a)

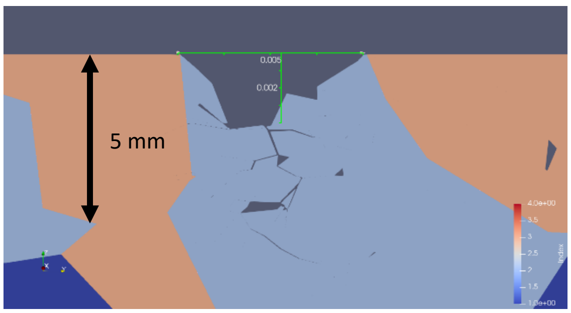

(b) $DI = 20\%$

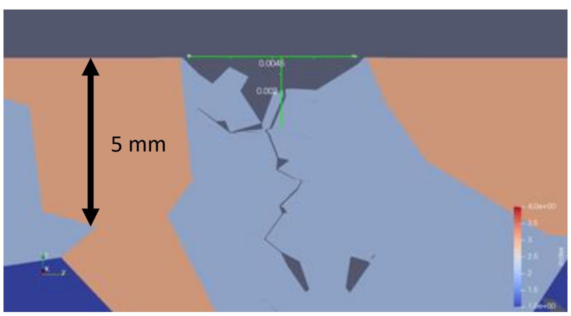

(c) $DI = 25\%$

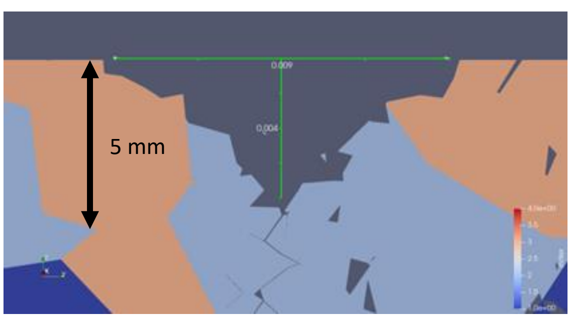

(d) $DI = 30\%$

Fig. 7. Calibration of Jetting Depth with Defect Intensity. (a) Displays 30% of all defects highlighted with black lines. (b), (c), and (d) illustrate models with Defect Intensity (DI) as given. The FDEM simulation results in the formation of discrete fragments and cracks (i.e., groove structures), which are visible as empty spaces against a grey background.

The algorithm to remove the fragments, leaving behind grey space, does not distinguish broken rock that is not connected to the free surface from that which is connected, hence the deep ‘holes’ shown when using the earlier algorithm. In more recent work, a sophisticated algorithm is used to remove only those fragments that are not locked down to the main intact rock, while realistically allowing backpressure to suppress removal.

5. MODELLING JETTING OF SIDOBRE GRANITE

5.1. *Heterogeneity and Crystal Sizes with Respect to Jet Diameter – Non-Traversing Jet*

For non-traversing conditions, big differences in jettability arise depending on the crystals that lie in the target zone because at the jet scale the rock is highly heterogeneous.

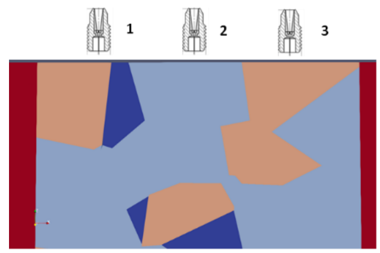

(a)

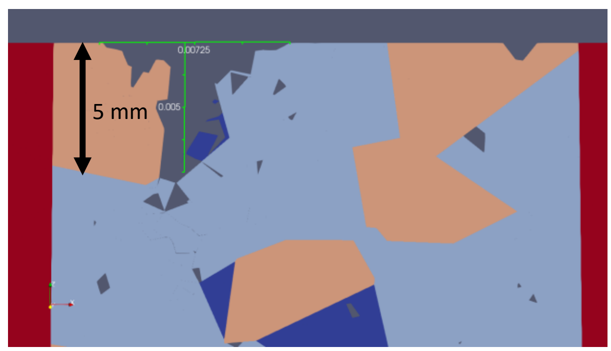

(b) Location 1

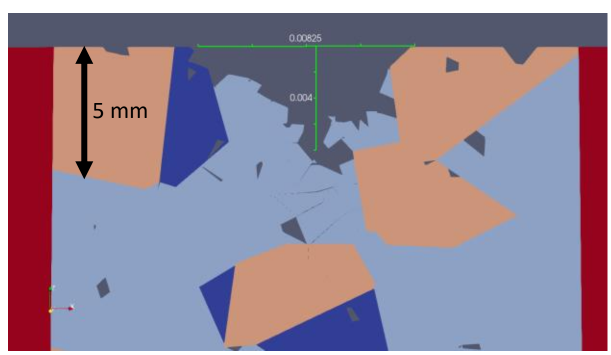

(c) Location 2

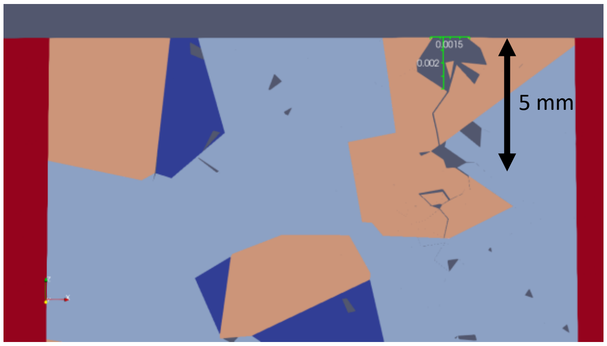

(d) Location 3

Fig. 8. 3D microstructure-based model simulation illustrating mineral fabric heterogeneity effect. (a) Cross-Sectional view for three jet impact locations. Samples were taken from different positions of jet impact: 1. Biotite/Quartz grain boundary area, 2. Feldspar, 3. Quartz and results are shown in (b), (c) and (d).

Figure 8 shows the set-up and illustrates the corresponding simulation results for different locations of the jet. The benchmark conditions modelled are: Confining pressure 20 MPa, Back pressure 20 MPa, Chamber pressure 240 MPa, Stand-off distance 3 mm, Nozzle diameter 1 mm. Note that the Defect Intensity was calibrated to be 30%.

Clearly, the jetting hole depth can be seen to vary considerably, the range captured here being between 6 mm (biotite boundary) and 2 mm (quartz) and this spread is compatible with the randomly repeated non-traversing jetting results shown in Figure 3. The numerical model appears to suggest that axial (or median) cracks tend to preferentially develop. One explanation for this is that the cracking is occurring because of the equivalent process to the "water hammer effect" as postulated for the relative effectiveness of pulsating water jets as compared with continuous jets.

In Section 4.2, the model is arranged with the jet striking the middle of a feldspar grain and this is perhaps a good starting point for the calibration case as the feldspars occupy well over half of the rock's constituents. In considering the effect of a traversing jet, the model boundary conditions are set up to have the appropriate jet pressure distribution displaced at a steady velocity of 157 mm/s. This velocity corresponds to the bit rotation speed of 20 RPM and a jet located 75 mm from the centre, the nozzle distance set up in the pressure cell jetting tests.

5.2. *Starting Point Effect – Traversing Jet*

In the first traversing simulations, we investigate the difference made by the starting point selected for the simulation. The boundary conditions are as schematically shown in Figure 6 except the jet pressure boundary condition is traversing at 0.157 m/s from left to right.

The consistency between the two distinct results for different starting points giving groove depths of 4.5 mm and 6 mm, as depicted in Figure 9, is highly reassuring. This agreement with the experimental data, (Figure 4) which shows a range from 3.8 mm to 5.2 mm, suggests that starting point effects and inherent heterogeneity provide plausible explanations for the observed variability in the experimental data. In Figure 9 the simulation of fragment removal is giving pitting and more irregular rock resistance/retention compared with the real experiments (Figures 5 and 9). Fluid flows, not fully included in the simulation, are contributing to a somewhat smoother erosive action and crater form. However, the simulations do appear to be giving an excellent insight into the jetting process as seen in experiments when a complete revolution of the jet is examined, see Figure 5. For this experimental irregular shaped intermittent groove, when measured over 253 mm of traverse, the average section area A_{av} removed was 40.48 mm^2, average width W_{av} 16.3 mm and in accordance with average profile geometries, the effective average depth assuming $d_{eff} = 0.754 \sqrt{A_{av}}$ was 4.81 mm, self-consistent with the short traverse tests used in the validation study. The very short traverse simulations reported here are in good agreement with all the experimental data.

Note that it is largely a coincidence that the jetting depth is of a similar magnitude or only slightly greater than for the non-traversing cases simulated, since about 3 times less jet energy has been applied in the case of the traversing jet over its 10 mm path.

It is interesting to speculate on the reasons why the traversing jet would be more effective. Dehkhoda and Hood (2013) investigated pulsed jets and described the water hammer effect in jet rock interaction in submerged conditions. It has been suggested by Xiang et al. (2022) that a water-hammer effect simulated by their physics-based fluid-solid coupled model was responsible for the rock destruction seen when simulating submerged jet drilling in a weak porous sandstone. In the work reported here, the simulation applies a pressure boundary condition that varies in time and space to an impermeable rock. It seems reasonable to suggest that the effect of the jet core's relatively sudden arrival on new rock surface (and change in local state of stress) is captured by the transient dynamics of the FDEM solver. However, the impact of the pressure history profile and its relationship with a supposed "water hammer effect" is a subject requiring much further investigation. It is to be expected (in terms of jet energy arriving per unit length traversed) that the model would show an increase in average depth of groove for 10 RPM (i.e. 79 mm/s for the 75 mm radial distance of the jet from the ~210 mm diameter rock specimen centre, used in the pressure cell jet tests) compared to 20 RPM (157 mm/s) as seen in experiments (Figures 5 and 9). A maximum depth would most likely occur somewhere between 0 mm/s and this velocity of 10 m/s.

5.3. *Simulation of Confining Pressure Effect - Non-traversing Jet*

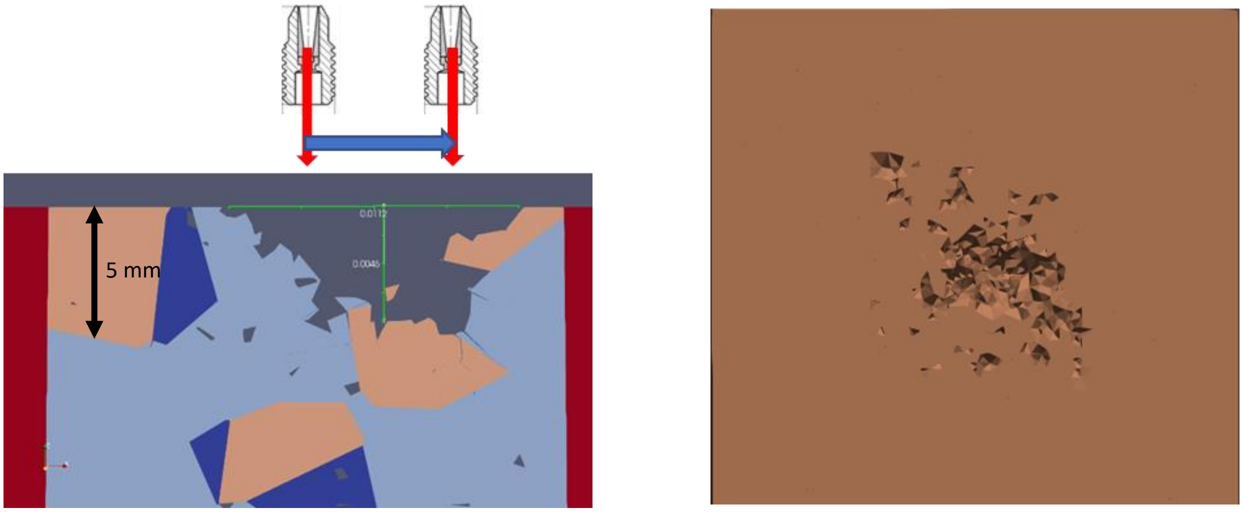

(a)

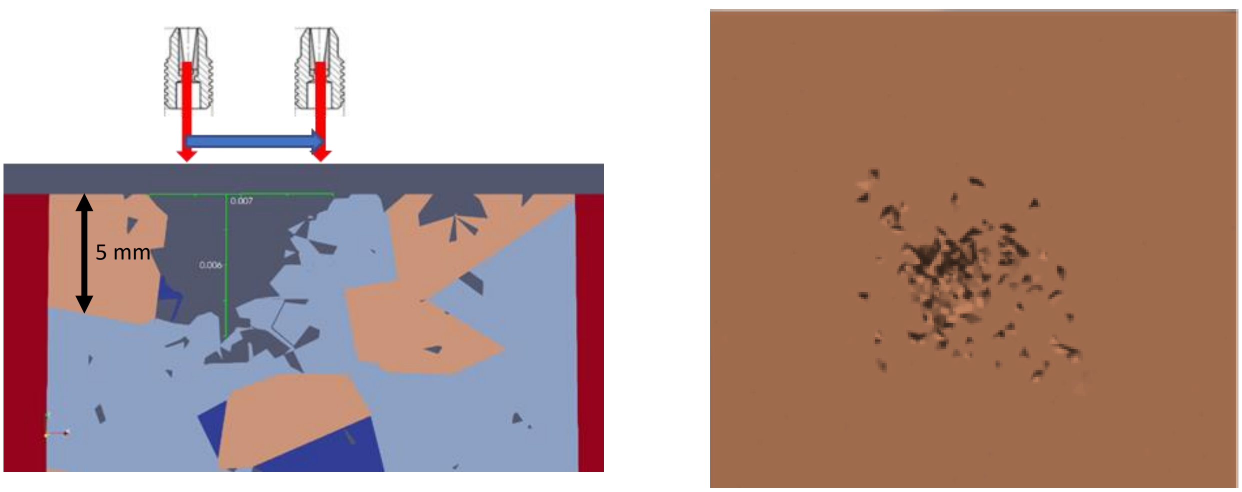

(b)

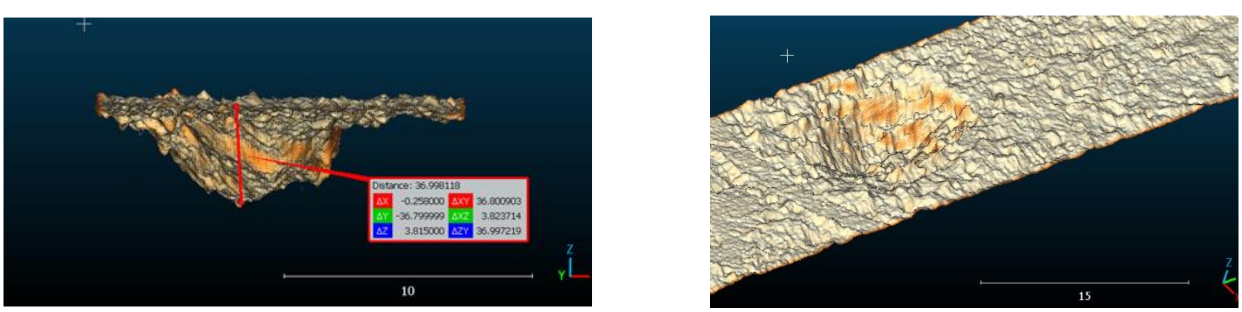

(c)

Fig. 9. Traversing Jet Model and Experimental Results. Jet traverse over approximately 5 mm at a velocity of 157 mm/s, tested with two different starting points. Cross-sectional views (left column) and top views (right column) depict the simulated grooves, both within the centre of feldspar (a) and aligned with the biotite/quartz boundary (b). (c) Two laser-scan visualisations (using software CloudCompare) of one corresponding short traversing jetting experiment (reported as TT2_4 in the data shared by ARMINES, pers comm), with crater length depth and shape of similar form to the simulated grooves but with a smoother less jagged jetted surface.

However, it is important to remember that in the context of hybrid HPWJ and rotating percussive drilling, the RPM requirement of a viable drilling system is likely to be for a drill rotation speed greater than 20 RPM for effective hammer action (e.g., 40-80 RPM). In this series of test simulations, we revert to a non-traversing jet and vary conditions from those of the benchmark case, effectively performing blind tests to examine the influence of different (hydrostatic) confining pressures.

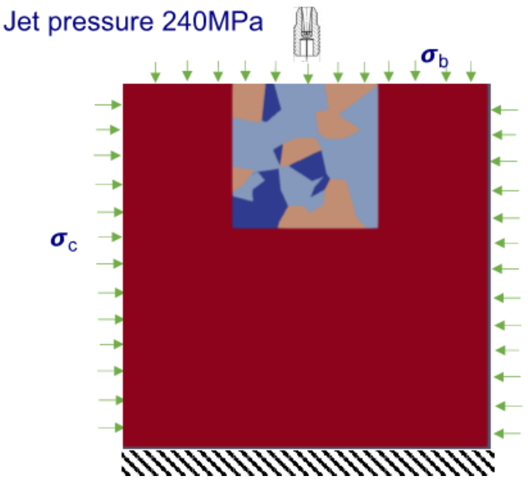

Fig. 10. Boundary conditions for the non-traversing jet model. Back pressure is set equal to confining pressure, σ_b = σ_c (i.e., hydrostatic state) with σ_c of 15 MPa, 20 MPa and 25 MPa.

In Figure 11, the meshed elements show the stress magnitude using the Von Mises stress measure with the hotter colours indicative of regions experiencing higher levels of shear stress. For σ_c = 15 MPa, the crater depth superficially appears not very deep but there are many highly stressed elements down to depths of ~7 mm. The crater width is 6.5 mm, and a moderate volume crater was produced. For σ_c = 20 MPa, the depth is just over 4 mm with somewhat less deeply penetrating damage than for 15 MPa. However, the crater width is 9.0 mm, and a larger fragment volume has been freed by the jet. For σ_c = 25 MPa, the higher shear stress magnitudes and cracking is still penetrating to about 5 mm, however the crater volume is much less than for the other two cases as fewer flaws and fresh cracks are creating fragments at the free surface of the crater. Insights from traversing (20 RPM, 157 mm/s) jet experiments e.g., see Fig. 5, where average groove profile areas and widths were evaluated from laser scan data confirm this trend, adding more detail. When increasing back pressure from 5 MPa to 20 MPa and then to about 40 MPa, the effective depths went from 6.7 mm to 5.0 mm to 0.8 mm, with effective widths of 16 mm, 16 mm and 5 mm respectively. Width to depth aspect ratio for this very coarse-grained granite went from 2.3 to 3.3 to 6.3, illustrating the very strong effect that pressure cell confinement pressures have in suppressing the depth of groove and rock volumes removed.

Further investigation into the role of elevated geostatic stress and anisotropic in-situ stress fields generally is required for the bottom hole geometry for each drillhole depth and back pressure constraint. In particular, at 50 MPa back pressure in 5 km deep holes, horizontal stresses of 125-130 MPa are to be considered. The far field in-situ vertical stress that is strongly channelled in the bottom hole environment and has been assumed to have a negligible influence in these simulations needs further consideration. However, a less expensive e.g., mesoscale model, is considered likely to be more appropriate to investigate such effects of the groove position in relation to the hole's bottom and walls and the non-uniform in-situ stress near the periphery.

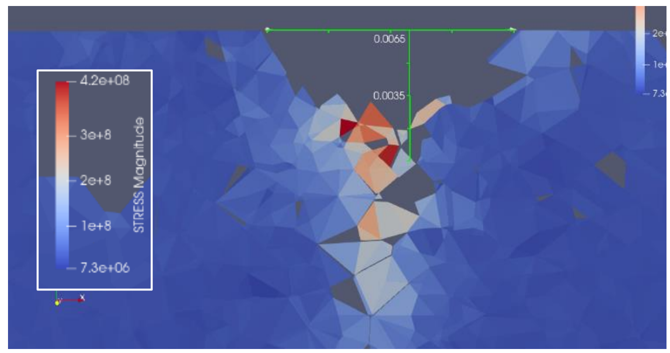

(a) $\sigma_c = 15$ MPa

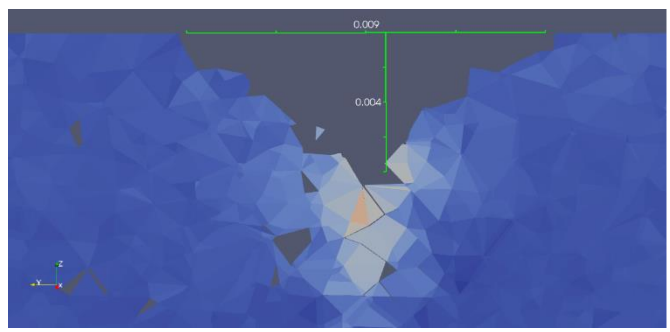

(b) $\sigma_c = 20$ MPa

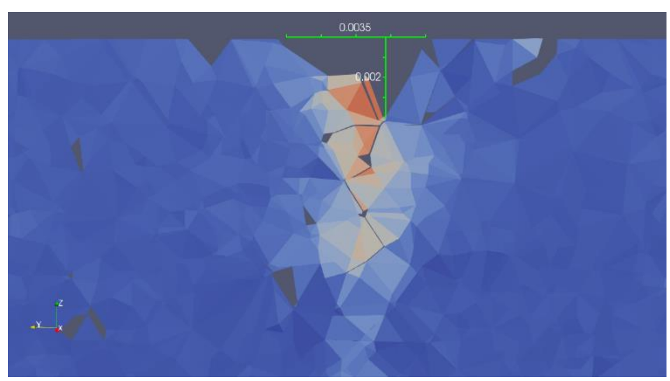

(c) $\sigma_c = 25$ MPa

Fig. 11. Microstructure-based jetting model with same region of SD granite and feldspar immediately below the jet impinging point in each case, showing effect of confining stress of 15, 20 and 25 MPa.

6. CONCLUSIONS

The microstructure of the Sidobre granite was characterised using a range of advanced experimental techniques. The micro-mechanical grain boundary and intra-grain properties, either measured or deduced, were assigned to the appropriately meshed FDEM model. A novel calibration process involving direct modelling of the load to failure of a 10 mm Brazilian disc laboratory experiment was introduced, together with nano-indentation testing.

Modifications to the Solidity FDEM code to simulate jetting action with a pressure boundary condition approach were made to maintain realistic pressure conditions as new fracture surface was generated in the crater walls. The pressure boundary can vary in space and time to allow the jet to traverse and act on the crater surfaces of eroding rock.

Benchmark experiments included non-traversing jetting tests were designed in collaboration with ARMINES and performed in Pau in the pressure cell. To simulate the jet's groove development and rock destruction for the Sidobre (SD) granite, using calibrated model micro-parameters that exploit the Brazilian disc tests, it was necessary to introduce a further material characteristic for this granite. The introduction of an adjustable Defect Intensity (DI) parameter, a catch-all term for flaws such as microcracks and defects, was investigated during the validation study using the benchmark experimental data set. For this rock, DI was set to a value of 30% to give a close agreement between simulation and experiment for the benchmark conditions.

The heterogeneity of the granite rock, which by definition is a coarse-grained crystalline igneous rock, when viewed from the scale of the 1 mm diameter impinging pressure zone of the HPWJ, is key to understanding the range of jet responses. It is why groove or crater depth varies so much between experimental tests on the same rock block. Sidobre granite is an especially coarse granite with feldspar crystals ranging from 2 to 10 mm. Depending on the jet starting point and therefore the crystalline topology and phases immediately beneath the jet, larger or smaller volumes of mineral are broken out.

The validated non-traversing model was applied to the case of a traversing nozzle moving at 157 mm/s and for a very small number of simulations and experiments the predicted depth of the groove was remarkably similar in range and mean values to those found in the experiments.

As the traversing jet is always striking new rock, we speculate that there is a water-hammer effect of the first massive increase in locally applied pressure when the rotating bit and jet first arrives over the rock surface that is otherwise mostly experiencing only the bottom hole back pressure. If the traversing speed is too fast, there is not enough energy to create the large change in pressure in a short time. If too slow, the regime is more like non-traversing where the pressure is very high but not changing with time after the initial arrival. There is likely to be a traversing speed that maximises groove depth. This is because grooves generated at 10 RPM were deeper than 20 RMP generated grooves but stationary jets dispensing three times the power of the 20 RPM generated grooves were of comparable depths to the 20 RPM grooves.

A first look at the effect of having greater confining pressure of 25 MPa suggests a potentially significant decrease in volume of material removed compared with the 20 MPa case. The modelling tool has great potential to investigate jetting at realistic and anisotropic stress states for hole depths of 4 to 5 km targeting geothermal resources.

ACKNOWLEDGEMENTS

This project was funded by the European Union's Horizon 2020 research and innovation programme under grant agreement no. 101006752.

REFERENCES

1. Dehkhoda, S. and Hood, M. (2013). An experimental study of surface and sub-surface damage in pulsed water-jet breakage of rocks. *International Journal of Rock Mechanics and Mining Sciences*, 63:138-147.
2. Dumoulin, S, Thenevin, I., Kane, A., Rouabhi, A., Latham, JP., Jahangir, E., Sellami, H. (2024). A complete experimental study on hard granites: microstructural characterization, mechanical response, and failure criterion. *Geomechanics for Energy and the Environment*, In review & revision.
3. Guo, L., Latham, JP., and Xiang., J. (2015). Numerical simulation of breakages of concrete armour units using a three-dimensional fracture model in the context of the combined finite-discrete element method. *Computers and Structures*, 146:117-142.
4. Guo, L., Xiang., J., Latham, JP., and Izzuddin B. (2016). A numerical investigation of mesh sensitivity for a new three-dimensional fracture model within the combined finite-discrete element method. *Engineering Fracture Mechanics*, 151:70-91.
5. Guo, L., Xiang., J., Latham, JP., and Izzuddin B. (2020). A generic computational model for three-dimensional fracture and fragmentation problems of quasi-brittle materials *European Journal of Mechanics-A/Solids*, 84: 104069.
6. Latham, J-P., Xiang, J., Gerbaud, L., Sellami, H., Naveen Velmurugan, N., Kane, A., Yang, J., Coudert, T., Liao, H. and Wang, H. (2022) Experimental and numerical investigation of high-pressure jetting fluids impinging on submerged hard rock under deep geothermal downhole drilling conditions. *European Geothermal Congress 2022*.
7. Lei, Q., Latham, J.P., Xiang, J., Tsang, C.F., Lang P. and Guo L. (2014). Effects of geomechanical changes on the

validity of a discrete fracture network representation of a realistic two-dimensional fractured rock. *International Journal of Rock Mechanics and Mining Sciences*, 70:507-523.

8. Mahabadi, O.K., Lisjak, A., Munjiza, A. and Graselli., G. (2012). Y-Geo: new combined finite-discrete element numerical code for geomechanical applications. *International Journal of Geomechanics*, 12(6):676-688.
9. Munjiza, A. (2004). The combined finite-discrete element method. John Wiley & Sons.
10. Stoxreiter, T., Portwood, G., Gerbaud, L., Seibel, O., Essl, S., Plank, J., Hofstätter, H., (2019). Full-scale experimental investigation of the performance of a jet-assisted rotary drilling system in crystalline rock. *International Journal of Rock Mechanics and Mining Sciences*,115, 87–98.
11. Xiang, J., Munjiza, A. and Latham J-P., (2009). Finite strain, finite rotation quadratic tetrahedral element for the combined finite–discrete element method. *International journal for numerical methods in engineering*, 2009. 79(8): 946-978.
12. Xiang, J., Chen, B. Latham, J-P. and Pain, C.C. (2022). Numerical simulation of rock erosion performance of a high-speed water jet using an immersed-body method. *International Journal of Rock Mechanics and Mining Sciences*, 2022. 158:105179.
13. Zhang, Y., Ngai, L. and Wong, Y. (2019). A review of numerical techniques approaching microstructures of crystalline rocks. Computers & Geosciences, 115:167-187.